

Magnetic Excitation of t - J Model with Quasi-One-Dimensional Fermi Surface — Possible Relevance to LSCO Systems

Hiroyuki Yamase¹ and Hiroshi Kohno²

¹*Institute for Solid State Physics, University of Tokyo,
5-1-5 Kashiwanoha, Kashiwa, Chiba 277-8581, Japan*

²*Graduate School of Engineering Science,
Osaka University, Toyonaka, Osaka 560-8531, Japan*

(Dated: May 14, 2001)

Abstract

On the basis of the picture of a quasi-one-dimensional (q-1d) Fermi surface (FS), recently proposed by authors for LSCO systems, spin excitation spectrum, $\text{Im}\chi(\mathbf{q}, \omega)$, is calculated in the ‘RPA’ within the slave-boson mean-field approximation to the t - J model. It is found that $\text{Im}\chi(\mathbf{q}, \omega)$ shows both incommensurate (IC) and diagonal IC (DIC) peaks, whose realization does not depend on the existence of the d -wave gap. The peak positions do not change appreciably with ω and the sharp peaks survive down to the low hole doping rate. The d -wave gap suppresses both the IC peak and the DIC peak, but the degree of suppression as a function of ω is different between them. Taking these results together with results for the two-dimensional FS, we argue that essential features of magnetic excitation in LSCO systems can be understood in terms of the q-1d picture of the FS.

PACS numbers:

I. INTRODUCTION

Recently, elastic neutron scattering¹⁻⁴ and hard X-ray scattering^{5,6} for $\text{La}_{1.6-x}\text{Nd}_{0.4}\text{Sr}_x\text{CuO}_4$ (LNSCO) have revealed four superlattice peaks at $(0, \pm 4\pi\eta)$ and $(\pm 4\pi\eta, 0)$ ⁷. These peaks are believed to come from some possible charge density modulation (CDM), accompanied by the magnetic incommensurate peaks at $(\pi, \pi \pm 2\pi\eta)$ and $(\pi \pm 2\pi\eta, \pi)$ at lower temperature. Here the ‘incommensurate’ means that the magnetic peak position is away from the commensurate position, (π, π) , and the value of η is called as incommensurability. This experimental data has been often discussed in terms of the so-called ‘spin-charge stripes’ hypothesis^{1,2}. In this hypothesis, one-dimensional (1d) charge order (or its fluctuations), namely ‘charge stripes’, is assumed in each CuO_2 plane and is considered to be essential to the realization of the incommensurate magnetic order (or its fluctuations); the direction of ‘charge stripes’ is assumed to alternate along the c -axis to explain the ‘observed’ four superlattice peaks.

On the theoretical side, some studies consider the ‘spin-charge stripes’ picture as a mechanism of superconductivity^{8,9}, and others use it to explain characteristic features of LSCO systems¹⁰⁻¹². The possible formation of ‘spin-charge stripes’, however, has not been clarified and has been one of the hot theoretical issues.

On the other hand, considering that some possible CDM has been indicated only in LNSCO with $x = 0.10, 0.12, 0.15$ ⁴, and neither in LNSCO with other hole density nor in other high- T_c cuprates such as $\text{La}_{2-x}\text{Sr}_x\text{CuO}_4$ (LSCO) and $\text{YBa}_2\text{Cu}_3\text{O}_{6+y}$ (YBCO), we have performed theoretical study¹³⁻¹⁵ under the assumption of uniform charge density, leaving a possible formation of some kind of CDM to a future study. As a result, we have proposed¹³ another possible picture for LSCO systems, a quasi-one-dimensional (q-1d) picture of the Fermi surface (FS). This is illustrated in Fig. 1: either of two kinds of the FSs, q-1dFS(x) or q-1dFS(y), is realized in each CuO_2 plane and they are stacked alternately along the c -axis. On the basis of this picture, we have argued that the apparently contradicting experimental results between the angle-resolved photoemission spectroscopy (ARPES)¹⁶ and the inelastic neutron scattering¹⁷ will be reconciled. As a microscopic support for the q-1d picture for LSCO systems, we have shown the followings^{14,15}. (1) The two-dimensional (2d) (spatial isotropic) t - J model has an intrinsic instability toward the formation of the q-1dFS at low temperature and this instability is most enhanced for the band parameters

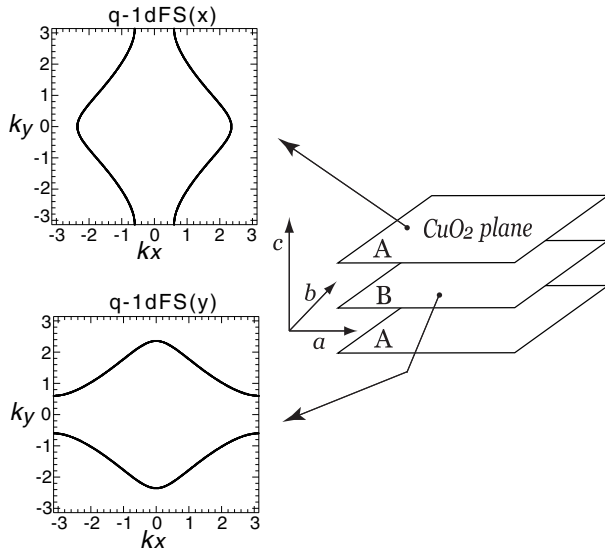


FIG. 1: Proposed quasi-one-dimensional picture of the FS. Either of two kinds of FSs, the q-1dFS(x) or the q-1dFS(y), is realized in each CuO_2 plane and they are stacked alternately along the c -axis.

appropriate to LSCO systems. (2) The q-1d instability is, however, usually masked by the more prominent d -wave pairing instability. (3) Nonetheless, the presence of small extrinsic spatial anisotropy is sufficient for the q-1d state to manifest in the d -wave pairing state; as an origin of such anisotropy in LSCO systems, we may assume the lattice distortion due to the low-temperature tetragonal (LTT) structure^{18–20} or its fluctuations^{21–23}. (The q-1d instability of the FS, as well as its competing nature with d -wave pairing instability, has independently been found in the Hubbard model also by Halboth and Metzner²⁴.)

In this paper, we perform a detailed study of magnetic excitation in the framework of the q-1d picture of the FS. Taking the q-1dFS consistent with ARPES results¹⁶, we calculate the dynamical spin susceptibility, $\chi(\mathbf{q}, \omega)$, especially $\text{Im}\chi(\mathbf{q}, \omega)$, in the ‘RPA’ within the slave-boson mean-field approximation to the t – J model. We first focus on the calculations for the single CuO_2 plane and neglect the interlayer coupling. After describing the formalism in §2, we show in §3.1 $\text{Im}\chi(\mathbf{q}, \omega)$ at low temperature where the d -wave singlet resonating-valence-bond (d -RVB) state is realized. At the same temperature we also perform the calculations assuming the uniform RVB (u-RVB) state (the state without the d -wave gap) and study effects of the d -wave gap (§3.2). Effects of the interlayer hopping (the formalism being given in Appendix A) and thermal fluctuations are investigated in §3.3 and §3.4, respectively. We

also study in §3.5 magnetic excitation for the 2dFS. Taking these results, we argue in §4 that essential features of magnetic excitation in LSCO systems can be understood in terms of the present q-1d picture of the FS. Our argument is different from the ‘spin-charge stripes’ scenario¹⁻³ where it is the formation of ‘charge stripes’, not effects of the FS, that gives rise to the magnetic incommensurate peaks.

II. MODEL AND FORMALISM

In this section, we give a formalism for a single CuO_2 plane. The case with the interlayer hopping is described in Appendix A.

A. Mean-field Hamiltonian

As a theoretical model of high- T_c cuprates, we take the 2d t - J model defined on a square lattice:

$$H = - \sum_{i,j,\sigma} t^{(l)} f_{i\sigma}^\dagger b_i b_j^\dagger f_{j\sigma} + J \sum_{\langle i,j \rangle} \mathbf{S}_i \cdot \mathbf{S}_j, \quad (1)$$

$$\sum_{\sigma} f_{i\sigma}^\dagger f_{i\sigma} + b_i^\dagger b_i = 1 \quad \text{at each site } i, \quad (2)$$

where $f_{i\sigma}$ (b_i) is a fermion (boson) operator that carries spin σ (charge e), namely we adopt the slave-boson scheme. $t^{(l)}$ is the hopping integral between the l -th neighbor sites i and j ($l \leq 3$), $J > 0$ is the superexchange coupling between the nearest neighbor spins, and $\mathbf{S}_i = \frac{1}{2} \sum_{\alpha,\beta} f_{i\alpha}^\dagger \boldsymbol{\sigma}_{\alpha\beta} f_{i\beta}$ with Pauli matrix $\boldsymbol{\sigma}$. The constraint eq. (2) excludes double occupations at every site.

The q-1dFS can be determined as a fully self-consistent solution by introducing some small spatial anisotropy in the t - J model¹⁴. The resulting q-1dFS, however, is not quantitatively consistent with ARPES data at each δ . In this paper, we aim at a *semiquantitative* study of magnetic excitations in LSCO systems based on the FS consistent with the ARPES results¹⁶. Therefore, rather than sticking to such self-consistent treatment, we take the following phenomenological procedure to reproduce the FS consistent with FS segments observed by ARPES at each δ .

We introduce the mean fields: $\chi^{(l)} \equiv \langle \sum_{\sigma} f_{i\sigma}^\dagger f_{j\sigma} \rangle$, $\langle b_i^\dagger b_j \rangle$ and $\Delta_\tau \equiv \langle f_{i\uparrow} f_{i+\tau\downarrow} - f_{i\downarrow} f_{i+\tau\uparrow} \rangle$, where each is taken to be a real constant independent of lattice coordinates, and τ represents

the nearest neighbor bond direction, namely $\tau = x$ or y . The local constraint eq. (2) is loosened to a global one, $\sum_i (\sum_\sigma f_{i\sigma}^\dagger f_{i\sigma} + b_i^\dagger b_i) = N$, with N being the total number of lattice sites. We then decouple the Hamiltonian eq. (1) to obtain

$$H_{\text{MF}} = \sum_{\mathbf{k}, \sigma} \xi_{\mathbf{k}} f_{\mathbf{k}\sigma}^\dagger f_{\mathbf{k}\sigma} + \sum_{\mathbf{k}} \Delta_{\mathbf{k}} \left(f_{-\mathbf{k}\downarrow}^\dagger f_{\mathbf{k}\uparrow}^\dagger + f_{\mathbf{k}\uparrow} f_{-\mathbf{k}\downarrow} \right), \quad (3)$$

where

$$\xi_{\mathbf{k}} = (F_x \cos k_x + F_y \cos k_y) + F' \cos k_x \cos k_y + F'' (\cos 2k_x + \cos 2k_y) - \mu, \quad (4)$$

$$\Delta_{\mathbf{k}} = -\frac{3}{4} J \Delta_0 (\cos k_x - \cos k_y), \quad (5)$$

$$F_x = F_y = -2 \left(t^{(1)} \langle b_i^\dagger b_j \rangle + \frac{3}{8} J \chi^{(1)} \right), \quad (6)$$

$$F' = -4t^{(2)} \langle b_i^\dagger b_j \rangle, \quad F'' = -2t^{(3)} \langle b_i^\dagger b_j \rangle, \quad (7)$$

$$\Delta_0 \equiv \Delta_x = -\Delta_y, \quad (8)$$

and μ is the chemical potential. We neglect boson degree of freedom, assuming the condensation to the bottom of its band. This assumption will be reasonable at low temperature and leads to $\langle b_i^\dagger b_j \rangle \approx \delta$.

Focusing our attention on LSCO systems, we take band parameters as²⁵ $t^{(1)}/J = 4$, $t^{(2)}/t^{(1)} = -1/6$ and $t^{(3)}/t^{(1)} = 0$, and determine mean fields self-consistently. The resulting ‘2dFS’ turns out to reproduce the observed FS¹⁶ in LSCO with $\delta = 0.30$ ²⁶, but not with lower δ ($\lesssim 0.22$). In order to reproduce the FS on the basis of the q-1d picture of the FS shown in Fig. 1, we reduce for the q-1dFS(x) the value of F_y at each δ , keeping the other parameters, F_x , F' , F'' , μ and Δ_0 , fixed:

$$F_y = \alpha F_x \quad (0 < \alpha \leq 1). \quad (9)$$

The value of α is chosen to adjust our theoretical q-1dFS(x) near $(0, \pi)$ to the observed FS segments¹⁶. The obtained values are plotted in Fig. 2: the band anisotropy decreases with increasing δ and eventually disappears at $\delta = 0.30$ where the ‘2dFS’ is realized. Note that the ‘2dFS’ was used for discussing the LSCO systems in the previous theory^{25,27}. Hence, the present theory recovers the previous one at high δ .

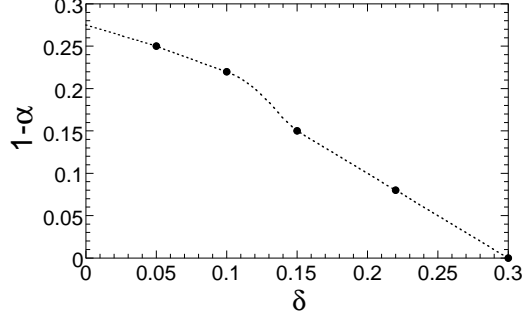


FIG. 2: The band anisotropy, $1 - \alpha$, determined by adjusting the q-1dFS to the observed FS segments for several choices of δ . The dotted line is drawn smoothly so as to estimate α at each δ .

B. Dynamical magnetic susceptibility

Using the mean-field Hamiltonian, eq. (3), we calculate the irreducible dynamical magnetic susceptibility as

$$\chi_0(\mathbf{q}, \omega) = \frac{1}{4N} \sum_{\mathbf{k}} \left[C_{\mathbf{k}, \mathbf{k}+\mathbf{q}}^+ \left(\tanh \frac{\beta E_{\mathbf{k}}}{2} - \tanh \frac{\beta E_{\mathbf{k}+\mathbf{q}}}{2} \right) \frac{1}{E_{\mathbf{k}} - E_{\mathbf{k}+\mathbf{q}} + \omega + i\Gamma} + \frac{1}{2} C_{\mathbf{k}, \mathbf{k}+\mathbf{q}}^- \left(\tanh \frac{\beta E_{\mathbf{k}}}{2} + \tanh \frac{\beta E_{\mathbf{k}+\mathbf{q}}}{2} \right) \left(\frac{1}{E_{\mathbf{k}} + E_{\mathbf{k}+\mathbf{q}} + \omega + i\Gamma} + \frac{1}{E_{\mathbf{k}} + E_{\mathbf{k}+\mathbf{q}} - \omega - i\Gamma} \right) \right] \quad (10)$$

where $\beta^{-1} = T$ is temperature and

$$E_{\mathbf{k}} = \sqrt{\xi_{\mathbf{k}}^2 + \Delta_{\mathbf{k}}^2}, \quad (11)$$

$$C_{\mathbf{k}, \mathbf{k}+\mathbf{q}}^{\pm} = \frac{1}{2} \left(1 \pm \frac{\xi_{\mathbf{k}} \xi_{\mathbf{k}+\mathbf{q}} + \Delta_{\mathbf{k}} \Delta_{\mathbf{k}+\mathbf{q}}}{E_{\mathbf{k}} E_{\mathbf{k}+\mathbf{q}}} \right). \quad (12)$$

The value of Γ should be a positive infinitesimal, but here we set $\Gamma = 0.01J$, which may simulate finite lifetime of fermions.

The RPA dynamical magnetic susceptibility is then obtained as

$$\chi(\mathbf{q}, \omega) = \frac{\chi_0(\mathbf{q}, \omega)}{1 + 2rJ(\mathbf{q})\chi_0(\mathbf{q}, \omega)}, \quad (13)$$

where $J(\mathbf{q}) = J(\cos q_x + \cos q_y)$ and we introduce a numerical factor r for convenience. In this RPA, where $r = 1$, $\chi(\mathbf{q}, 0)$ diverges at low temperature in the wide doping-region $\delta \lesssim 0.17$ (in the d -RVB state). This magnetic instability will be an artifact, since such divergence of $\chi(\mathbf{q}, 0)$ will be suppressed by higher order corrections to $\chi_0(\mathbf{q}, \omega)$. This aspect we take into

account phenomenologically by reducing the value of r to 0.35. As a result, the divergence of $\chi(\mathbf{q}, 0)$ is limited to the region $\delta \lesssim 0.02$ (0.05) in the d -RVB (u-RVB) state.

III. RESULTS

We first present the calculations for a single CuO_2 plane and show the \mathbf{q} -dependence of $\text{Im}\chi(\mathbf{q}, \omega)$ for the q-1dFS(x); temperature is set to $T = 0.01J$ where the d -RVB state is stabilized. We also calculate $\text{Im}\chi(\mathbf{q}, \omega)$ assuming the u-RVB state at the same temperature and study effects of the d -wave gap; mean-field parameters in the u-RVB are determined self-consistently within a manifold of $\Delta_0 \equiv 0$, and the same value is taken for α as that in the d -RVB state. We next investigate effects of the interlayer hopping and thermal fluctuations. Finally we compare results for the q-1dFS with those for the 2dFS. In the following, we take J as an energy unit.

A. \mathbf{q} -dependence of $\text{Im}\chi(\mathbf{q}, \omega)$

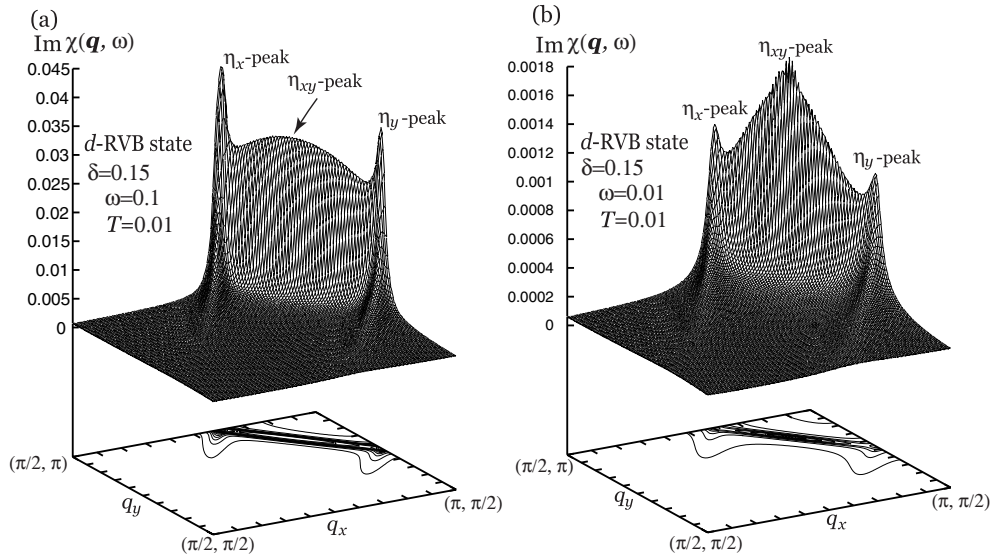


FIG. 3: \mathbf{q} -dependence of $\text{Im}\chi(\mathbf{q}, \omega)$ at $\omega = 0.1$ (a) and 0.01 (b) in the d -RVB state. The contour lines are projected on the \mathbf{q} -plane. In (b), the fine structure around the η_{xy} -peak is due to the coarse mesh in the plot and should be understood with a smooth interpolation.

In Fig. 3(a), we show the \mathbf{q} -dependence of $\text{Im}\chi(\mathbf{q}, \omega)$ at $\omega = 0.1$ in the region $\frac{\pi}{2} \leq q_x, q_y \leq \pi$ together with the projected contour-lines on the \mathbf{q} -plane. The overall structure of $\text{Im}\chi(\mathbf{q}, \omega)$ is almost 2d-like even in the state with the q-1dFS(x), except for the absence of the exact tetragonal symmetry, $(q_x, q_y) \rightarrow (\pm q_y, \pm q_x)$. There exist two different incommensurate (IC-) peaks at $(\pi - 2\pi\eta_x, \pi)$ and $(\pi, \pi - 2\pi\eta_y)$, which we call the η_x -peak and the η_y -peak, respectively. These peaks are connected with each other by a ‘wall’, as seen from the dense contour lines in Fig. 3(a). The center of the ‘wall’ located at $(\pi - 2\pi\eta_{xy}, \pi - 2\pi\eta_{xy})$ forms a local maximum or a diagonal IC (DIC-) peak, which we call the η_{xy} -peak. With decreasing ω , the η_x, η_y -peaks are rapidly suppressed compared with the η_{xy} -peak, and the latter then becomes dominant as shown in Fig. 3(b).

These structures of $\text{Im}\chi(\mathbf{q}, \omega)$ can be understood in terms of fermiology as follows. In the present q-1dFS(x), ‘ $2k_F$ ’-scattering vectors are located on the gray lines in Fig. 4. Along this gray line $\text{Im}\chi(\mathbf{q}, \omega)$ shows the ‘wall’ structure, and the locations of the η_{xy} -peak are denoted by ‘+’ and those of the η_x, η_y -peaks by the open symbols. Since the same open

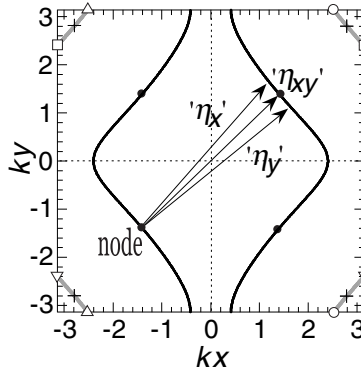


FIG. 4: Typical particle-hole scattering processes for the q-1dFS(x) in the d -RVB state. (The FS is drawn by setting $\xi_{\mathbf{k}} = 0$, but note that the band dispersion is given by $E_{\mathbf{k}} = \sqrt{\xi_{\mathbf{k}}^2 + \Delta_{\mathbf{k}}^2}$. The d -wave gap nodes on the FS are denoted by the filled circles.) The gray line indicates the positions of ‘ $2k_F$ ’-scattering vectors connecting the vicinities of the d -wave gap nodes. The ‘+’ and the open symbols denote the location of the η_{xy} -peak and the η_x, η_y -peaks, respectively. The same open symbols indicate that they are connected by the reciprocal lattice vectors. The main scattering vectors for the η_x -peak (denoted by ‘ η_x ’), the η_{xy} -peak (‘ η_{xy} ’) and the η_y -peak (‘ η_y ’) are shown explicitly.

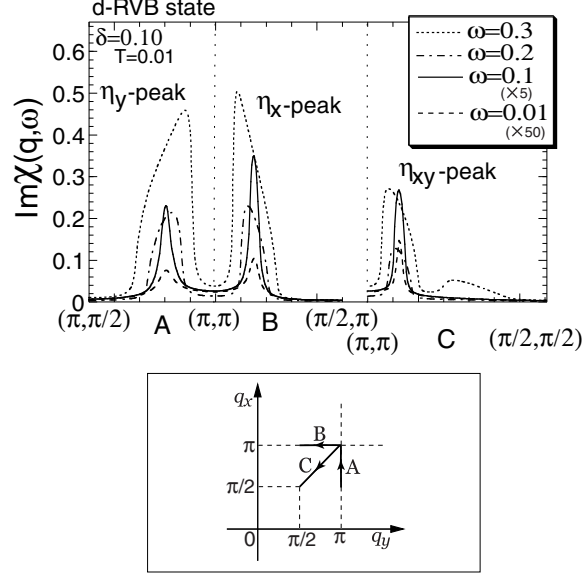


FIG. 5: \mathbf{q} -dependence of $\text{Im}\chi(\mathbf{q}, \omega)$ in the d -RVB state at several values of ω along the direction shown in the lower panel. $\text{Im}\chi(\mathbf{q}, \omega)$ at $\omega = 0.1$ and 0.01 are multiplied by 5 and 50, respectively.

symbols are connected by the reciprocal lattice unit, Umklapp processes also contribute to the η_x, η_y -peaks. We show in Fig. 4 the main scattering processes for each peak around (π, π) . (Umklapp processes are not shown.) Each scattering process originates from the d -wave gap node. In particular, the η_{xy} -peak results from the scattering between the d -wave gap nodes. This is why the η_{xy} -peak becomes dominant at lower ω .

To see the ω -dependence of $\text{Im}\chi(\mathbf{q}, \omega)$ more clearly, we perform the \mathbf{q} -scan along three lines, each of which is across the η_x -peak, the η_y -peak or the η_{xy} -peak, respectively, and show the result in Fig. 5 for several choices of ω at $\delta = 0.10$. With increasing ω , the peak becomes broader and the η_x, η_y -peaks develop more rapidly than that of the η_{xy} -peak. The location of each peak does not change appreciably up to $\omega \sim 0.2$ and shifts toward (π, π) at larger ω . This insensitivity to ω is weakened for lower δ and is limited to $\omega \lesssim 0.1$ at $\delta = 0.05$.

In Fig. 6, we show the δ -dependence of $\text{Im}\chi(\mathbf{q}, \omega)$ at $\omega = 0.01$. Both the η_x, η_y -peaks and the η_{xy} -peak remain sharp down to low δ . The latter develops at lower δ relative to the former.

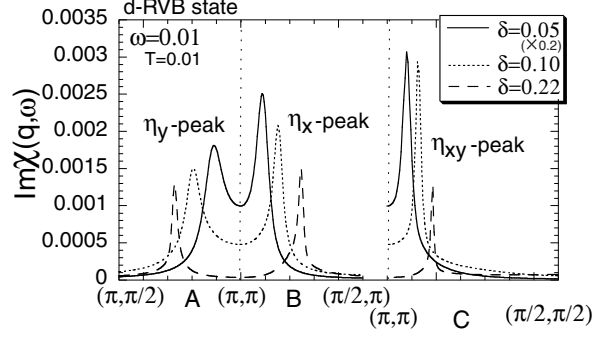


FIG. 6: \mathbf{q} -dependence of $\text{Im}\chi(\mathbf{q}, \omega)$ at $\omega = 0.01$ for several choices of δ in the d -RVB state. The result for $\delta = 0.05$ is multiplied by 0.2.

B. Effects of d -wave gap

To study effects of the d -wave gap, we show in Fig. 7 $\text{Im}\chi(\mathbf{q}, \omega)$ in the u-RVB state at several values of ω . As in the d -RVB state (Fig. 5), sharp peaks exist up to $\omega \sim 0.1$, although such ω -range is reduced compared with the d -RVB state, and the peak width gets broader. Hence, for the existence of the η_x, η_y -peaks and the η_{xy} -peak, the d -wave gap is not essential but the q-1dFS is. (In §3.5, we will see that for the 2dFS such sharp peaks are possible only in the d -RVB state.)

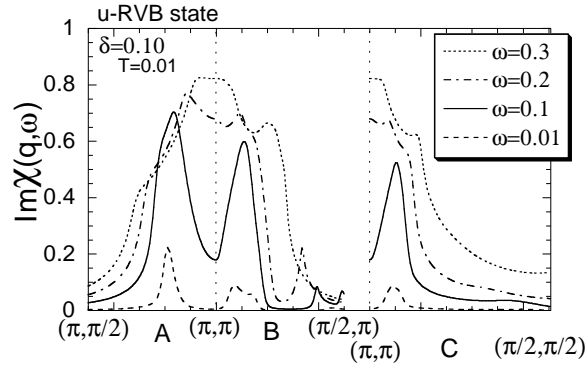


FIG. 7: \mathbf{q} -dependence of $\text{Im}\chi(\mathbf{q}, \omega)$ in the u-RVB state at several values of ω .

Figure 8 shows $\text{Im}\chi(\mathbf{q}, \omega)$ as a function of ω ; \mathbf{q} is fixed to the peak position, $\eta_y = 0.135$ (0.130) or $\eta_{xy} = 0.066$ (0.058), in the d -RVB (u-RVB) state for $\delta = 0.22$. Both the η_y -peak and the η_{xy} -peak are suppressed by the d -wave gap, because the d -wave gap reduces the density of states responsible to the low energy scattering. For the η_y -peak in the d -RVB,

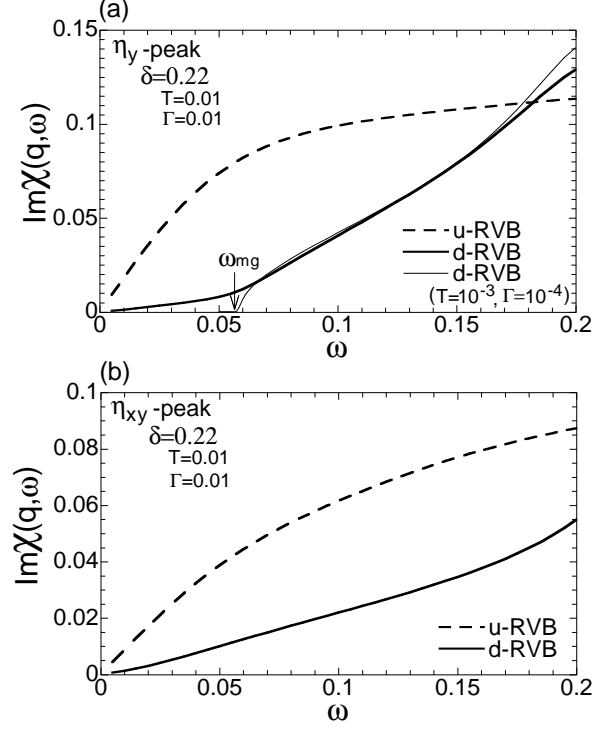


FIG. 8: ω -dependence of $\text{Im}\chi(\mathbf{q}, \omega)$ at \mathbf{q} corresponding to the η_y -peak (a) and the η_{xy} -peak (b) in the d -RVB state (solid line) and the u-RVB state (dashed line). The thin solid line in (a) is for lower temperature $T = 10^{-3}J$ and the smaller value of $\Gamma = 10^{-4}J$.

a gap-like behavior appears at low ω , and becomes clearer with decreasing both T and Γ as shown by the thin line ($T = 10^{-3}$ and $\Gamma = 10^{-4}$) in Fig. 8(a). This gap, which we call magnetic gap²⁸ ω_{mg} , is approximately given by

$$\omega_{\text{mg}}(\mathbf{q}) = E_{\mathbf{q}+\mathbf{k}_{\text{node}}}, \quad (14)$$

where \mathbf{q} is the scattering vector, $(\pi, \pi - 2\pi\eta_y)$, and \mathbf{k}_{node} is a d -wave gap node position on the FS. Since the η_{xy} -peak in the d -RVB results mainly from the scattering between the d -wave gap nodes (Fig. 4), the value of \mathbf{k}_{node} is estimated to be $-\frac{1}{2}(\pi - 2\pi\eta_{xy}, \pi - 2\pi\eta_{xy})$. Substituting the values of η_{xy} and η_y into eq. (14), we get $\omega_{\text{mg}}(\mathbf{q}) = 0.057$, which is in good agreement with Fig. 8(a). (This good agreement has also been checked for other hole density.) In Fig. 9, we plot $\omega_{\text{mg}}(\mathbf{q})$ as a function of δ together with the d -wave singlet order Δ_0 . Note the different δ -dependence between $\omega_{\text{mg}}(\mathbf{q})$ and Δ_0 . (In Appendix B, we give analytic formulae for estimating the values of η_{xy} and η_y . The magnitude of the magnetic gap is then obtained from eq. (14) without any calculations of $\text{Im}\chi(\mathbf{q}, \omega)$.)

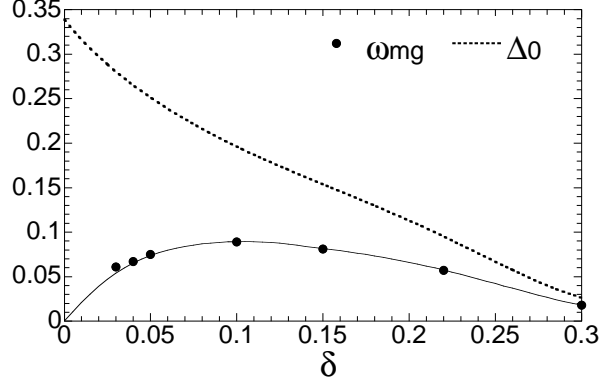


FIG. 9: The magnetic gap ω_{mg} (filled circle) at the η_y -peak as a function of δ . The solid line is drawn by using the analytic formulae, eqs. (14), (B1) and (B2). For comparison, the magnitude of the d -wave singlet order, Δ_0 , is also shown (dotted line).

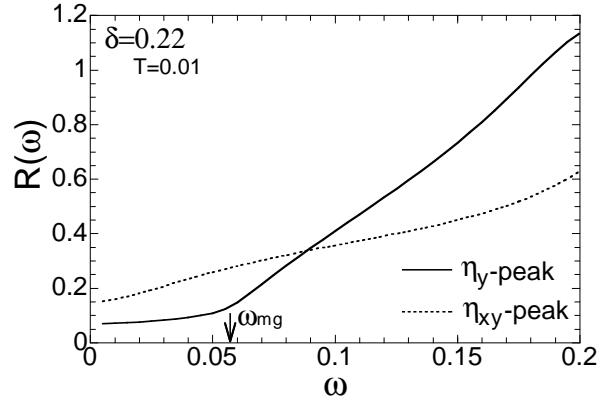


FIG. 10: The degree of suppression of the η_y -peak and the η_{xy} -peak by the d -wave gap as a function of ω . $R(\omega)$ is defined to be $\frac{\text{Im}\chi(\mathbf{q}, \omega)|_{d\text{-RVB}}}{\text{Im}\chi(\mathbf{q}, \omega)|_{u\text{-RVB}}}$ with \mathbf{q} corresponding to the peak position in each state.

On the other hand, the magnetic gap is zero at the η_{xy} -peak. This does not, however, mean that effects of the d -wave gap are smaller compared with the η_y -peak. Using the result shown in Fig. 8, we show in Fig. 10 the ratio,

$$R(\omega) = \frac{\text{Im}\chi(\mathbf{q}, \omega)|_{d\text{-RVB}}}{\text{Im}\chi(\mathbf{q}, \omega)|_{u\text{-RVB}}}, \quad (15)$$

for both the η_y -peak and the η_{xy} -peak as a function of ω . At $\omega \approx 0$, the d -wave gap suppresses the η_y -peak more strongly than the η_{xy} -peak. However, once ω exceeds ω_{mg} , the suppression of the η_{xy} -peak becomes more prominent than the η_y -peak.

C. Effects of interlayer hopping

Next, we investigate effects of the interlayer hopping, t_{\perp} , on the (single-layer) results presented so far. This introduces mixing between the two kinds of q-1d bands. Details of the formalism are given in Appendix A.

Reflecting the relative shift of Cu sites by $[\frac{1}{2}, \frac{1}{2}, \frac{1}{2}]$ (tetragonal notation) between the adjacent CuO_2 layers, the band dispersion along the k_z -direction is obtained as

$$\epsilon_{\mathbf{k}} = -8t_{\perp}\delta \cos \frac{k_x}{2} \cos \frac{k_y}{2} \cos \frac{k_z}{2}. \quad (16)$$

We set the interlayer transfer integral to be $t_{\perp} = 0.05t^{(1)}$ so that the band width of $\epsilon_{\mathbf{k}}$ is about 0.1 times that of $\xi_{\mathbf{k}}^{29}$. (We neglect the interlayer magnetic interaction, whose order is $\sim 10^{-5}J^{30-32}$.) In Fig. 11, we show the FS at $k_z = 0$ and π obtained by setting $\Delta_{\mathbf{k}} = 0$ in eq. (A9). The FS consists of the outer FS (solid line in Fig. 11) and the inner FS (gray line).

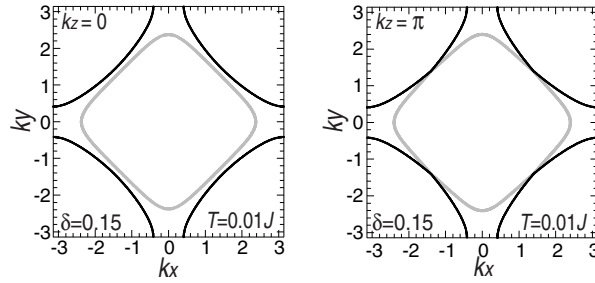


FIG. 11: Theoretical FS at $k_z = 0$ and π at low T in our quasi-one-dimensional picture of the FS in the presence of interlayer hopping. (see also Fig. 1.) The FS consists of the outer FS (solid line) and the inner FS (gray line).

Taking $q_z = 0$, we show in Figs. 12(a) and 12(b) the \mathbf{q} -dependence of $\text{Im}\chi(\mathbf{q}, \omega)$ at $\omega = 0.01$ for $\delta = 0.10$ and 0.22 (bold solid line) in the d -RVB state, comparing it with the (single-layer) result for the q-1dFS(x) (thin dotted line). The IC-peaks at $(\pi - 2\pi\eta_{\text{IC}}, \pi)$ and $(\pi, \pi - 2\pi\eta_{\text{IC}})$ remain sharp, and recover the fourfold symmetry around (π, π) . The peak position is almost the same as that of the (single-layer) η_x, η_y -peaks, and the width becomes slightly broader. On the other hand, the DIC-peak at $(\pi - 2\pi\eta_{\text{DIC}}, \pi - 2\pi\eta_{\text{DIC}})$ gets much broader compared with the (single-layer) η_{xy} -peak and is largely suppressed at high δ ($\gtrsim 0.22$).

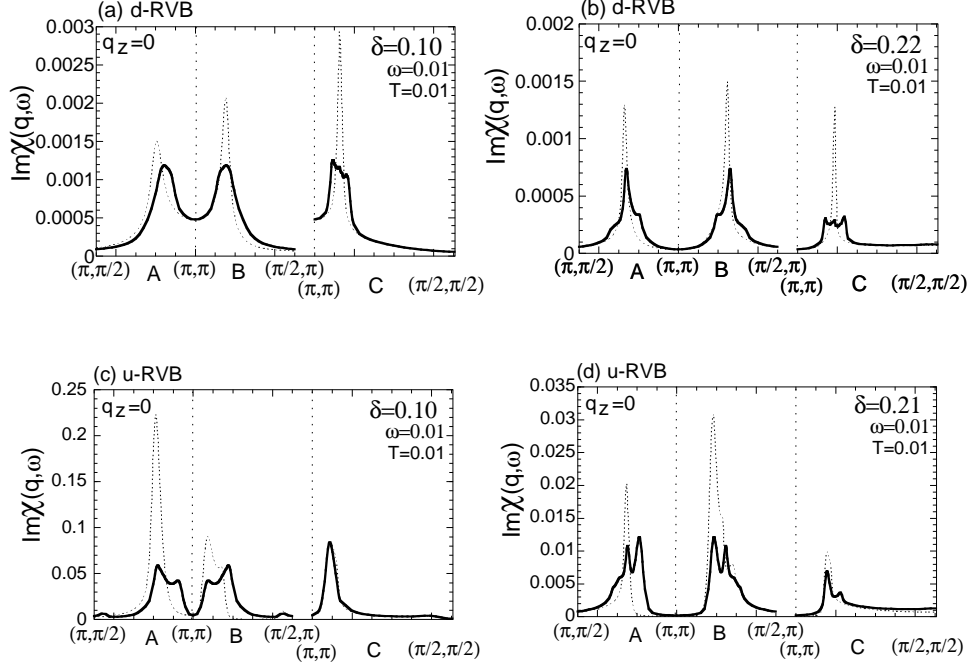


FIG. 12: \mathbf{q} -dependence of $\text{Im}\chi(\mathbf{q}, \omega)$ at $\omega = 0.01$ and $q_z = 0$ in the presence of interlayer hopping (solid lines). It is plotted in both the d -RVB state and the u -RVB state for several choices of δ . The rough topped DIC-peak in (a) and (b) will be due to the artifact of the present calculation and should be interpreted as a smooth one. (see the last paragraph in Appendix A.) The (single-layer) results for the q -1dFS(x) are also plotted for comparison (dotted lines).

Figures 12(c) and 12(d) show the results in the u -RVB state. As in the d -RVB, IC-peaks are seen, but the line shape changes qualitatively. The IC-peak has a hump on the (π, π) side at $\delta = 0.10$. This hump originates from the (single-layer) η_x -peak for the q -1dFS(x). Such structure develops into a double-peak structure at higher δ . With further increasing δ ($\gtrsim 0.23$), the double peaks merge into a single sharp peak because of the decrease of the band anisotropy, $\alpha \rightarrow 1$. As for the DIC-peak, the line shape is almost the same as that for the (single-layer) q -1dFS(x). The peak height relative to the IC-peak is suppressed at higher δ as in the case of the d -RVB.

With increasing ω , the IC-peak develops more rapidly than the DIC-peak, and become broader so that the fine structures such as the hump or the double-peak structure are smeared. These ω -dependence share the common features to the (single-layer) results shown in Figs. 5 and 7.

In Fig. 13, we plot the δ -dependence of η_{IC} and η_{DIC} at $\omega = 0.01$ in the d -RVB (a) and u -RVB (b) — the η_{DIC} at high δ is not shown since the peak height of the DIC-peak is less than 50% of the IC-peak. (For the low doping region $\delta \leq 0.05$ in the u -RVB, we take $r = 0.2$, instead of $r = 0.35$, to avoid magnetic instability in eq. (13).) In both states, the values of η_{IC} and η_{DIC} increase smoothly as a function of δ , except in the region $0.18 \lesssim \delta \lesssim 0.23$ in the u -RVB, where $\text{Im}\chi(\mathbf{q}, \omega)$ shows the double peaks. Their peak positions are plotted by filled circles with different size so that the smaller indicates the position of the lower peak. Since the relative height changes from the larger η_{IC} to the smaller η_{IC} in $0.19 \lesssim \delta \lesssim 0.21$ in Fig. 13(b), this may appear as a saturation behavior of η_{IC} in $0.15 \lesssim \delta \lesssim 0.20$.

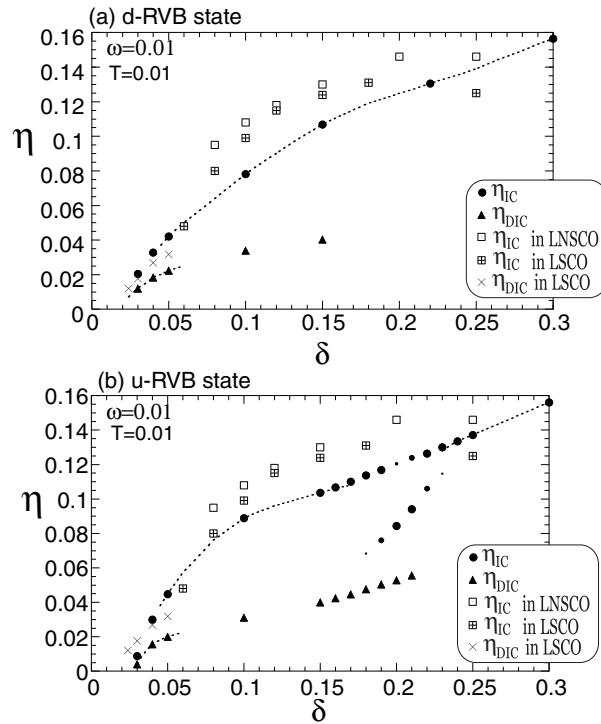


FIG. 13: Incommensurability, η_{IC} and η_{DIC} , as a function of δ for the d -RVB state (a) and the u -RVB state (b). In (b), two filled circles at each δ in the range $0.18 \leq \delta \leq 0.23$ correspond to the double-peak positions with the higher peak being indicated by the larger circle; the relative difference of the peak height is about 18% ($\delta = 0.18$), 2% ($\delta = 0.19$), 13% ($\delta = 0.20$), 10% ($\delta = 0.21$), 7% ($\delta = 0.22$), 17% ($\delta = 0.23$), respectively. Experimental data in LNSCO⁴⁷ and in LSCO^{17,50} are also plotted; note that the IC-peak has been reported in $\delta \geq 0.06$ and the DIC-peak in $\delta \leq 0.05$. The dotted lines are drawn for guides to the eye for comparison with experimental data.

At higher ω , the δ -dependence of η_{IC} and η_{DIC} in the d -RVB is almost the same as that at

$\omega = 0.01$, since the positions of the (single-layer) $\eta_x, \eta_y, \eta_{xy}$ -peaks do not change appreciably with ω as shown in Fig. 5. In the u-RVB state, however, the value of η_{IC} gets smaller especially in low δ ($\lesssim 0.15$) and possible saturation behavior in $0.15 \lesssim \delta \lesssim 0.20$ is smeared out. This qualitative difference from that at $\omega = 0.01$ is due to the smearing of the hump and the double-peak structures of $\text{Im}\chi(\mathbf{q}, \omega)$. In contrast, the value of η_{DIC} remains almost the same with increasing ω , as seen in the (single-layer) result shown in Fig. 7.

D. Temperature dependence of $\text{Im}\chi(\mathbf{q}, \omega)$

So far we have seen magnetic excitation at low T ($= 0.01J$). With increasing T , the following two effects may be expected. (i) The IC-peaks are thermally smeared out to form a C-peak. (ii) The q-1dFS is destabilized and is replaced by a ‘2dFS’. Here the possible ‘2dFS’ is the one obtained with the same band parameters as used in § 2.1, but $F_x = F_y$ is kept for each δ . The resulting FS at $\delta = 0.15$ is ‘electron-like’ centered at $(0, 0)$ as shown in Fig. 14.

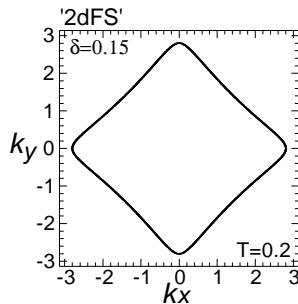


FIG. 14: The ‘2dFS’, which may be realized at high T in the present quasi-1d picture of the FS.

We thus calculate $\text{Im}\chi(\mathbf{q}, \omega)$ for several choices of T for both the q-1dFS and the ‘2dFS’ in the u-RVB state. We include the interlayer hopping and set $\omega = 0.1$ and $\delta = 0.15$. Figure 15 shows that the IC-peak exists for both FSs in $T \lesssim 0.1$. At $T = 0.2$, however, a broad C-peak is realized for the q-1dFS, and a weak IC-peak or an essentially flat topped commensurate (C-) peak for the ‘2dFS’.

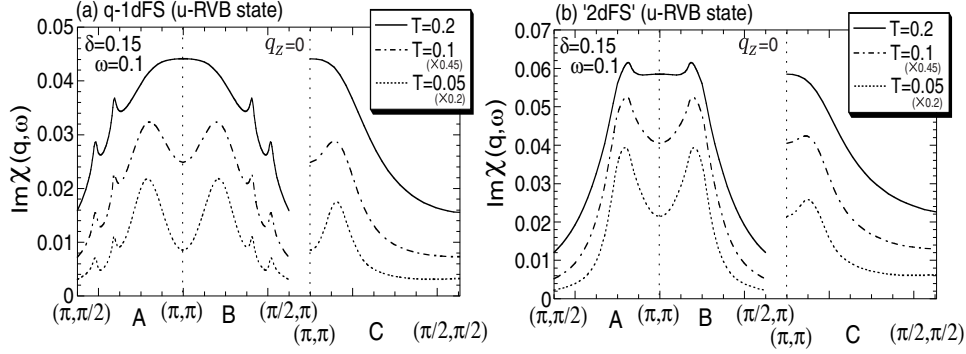


FIG. 15: \mathbf{q} -dependence of $\text{Im}\chi(\mathbf{q}, \omega)$ for several choices of T for the q-1dFS (a) and the ‘2dFS’ (b). Note that the interlayer hopping is included. The data at $T = 0.1$ and 0.05 are multiplied by 0.45 and 0.2 , respectively.

E. Comparison with 2dFS

As we discussed in the previous paper¹³, the present q-1d picture of the FS is consistent with the ARPES data in LSCO¹⁶. Moreover, recent data in ARPES³³, the \mathbf{k} -space distribution of low-energy spectral weight integrated down to 30meV below Fermi energy, has turned out to be consistent with our predicted FS shown in Fig. 11. We, however, note a different arguments from ours that the FS in LSCO will be the 2dFS shown in Fig. 16¹⁶. (Note the difference in topology from the ‘2dFS’ shown in Fig. 14.) We thus investigate the difference in magnetic excitation between the q-1dFS and the 2dFS here.

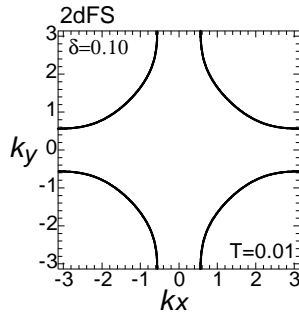


FIG. 16: The 2dFS discussed in the ARPES study for LSCO with $\delta \lesssim 0.20$ ¹⁶. This FS is different from the present quasi-one-dimensional picture. (see Figs. 1 and 11.)

We take the band parameters, $t^{(1)}/J = 4$, $t^{(2)}/t^{(1)} = -1/6$, and $t^{(3)}/t^{(1)} = 1/5$ and determine mean fields by minimizing the free energy in the same fashion as §2.1, but now

with $F_x = F_y$. We then obtain 2dFS shown in Fig. 16.

Using this 2dFS, we show $\text{Im}\chi(\mathbf{q}, \omega)$ for several choices of ω in Figs. 17(a) and 17(b). In the d -RVB, both the sharp IC-peak and the sharp DIC-peak are realized. In the u -RVB, however, a broad C-peak becomes dominant and the remnants of the IC,DIC-peaks appear as weak substructures. This feature contrasts with the case of the q -1dFS where the sharp IC,DIC-peaks are realized even in the u -RVB. This difference may be understood by noting that the 2dFS allows the scattering vector (π, π) from one point to the other on the FS while the q -1dFS does not. (When we introduce hybridization between the two kinds of the q -1d bands, the resulting FS (Fig. 11) allows such (π, π) scattering vectors. However, these scatterings occur through the interlayer hopping and do not contribute appreciably to $\text{Im}\chi(\mathbf{q}, \omega)$ as seen from Figs. 12(c) and 12(d).)

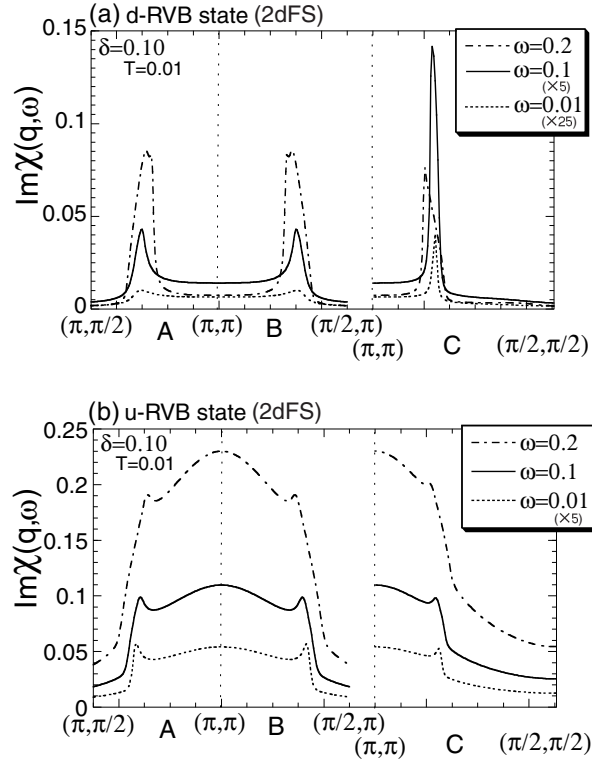


FIG. 17: \mathbf{q} -dependence of $\text{Im}\chi(\mathbf{q}, \omega)$ for several choices of ω for the 2dFS in the d -RVB state (a) and the u -RVB state (b). (The interlayer hopping is not included.) The data at $\omega = 0.1$ and 0.01 in (a), and the data at $\omega = 0.01$ in (b) are multiplied by 5, 25 and 5, respectively.

IV. DISCUSSION

A. Possible q-1d picture of FS in LSCO systems

Now we discuss a possible q-1d picture of the FS in LSCO systems from the viewpoint of magnetic excitation. We take the following four subjects: (i) IC-peak at high temperature, (ii) ω -dependence and magnetic gap, (iii) incommensurability versus hole density, and (iv) IC-peak versus DIC-peak.

1. IC-peak at high Temperature

Experimentally, the IC-peak has been observed at $T = 80\text{K}$ for LSCO with $\delta = 0.14$ ³⁴, and the spin gap behavior has not been observed at least above $T \approx 80\text{K}$ ^{35–38}. Thus it is difficult to understand such experimental data in terms of the 2dFS, since as shown in Fig. 17, the IC-peak for the 2dFS is realized only in the d -RVB state (with the spin gap), and is replaced by the essentially C-peak in the u -RVB state (without the spin gap). Rather, such experimental data is consistent with the results based on the q-1d picture of the FS as shown in Figs. 7, 12(c), 12(d), 15(a) and 15(b), where IC-peaks have been realized in the u -RVB state at least for $T \lesssim 0.1J$; the value of J is estimated as $\sim 135\text{meV}$ ³².

The data in ref. 34 also indicates a weak IC-peak (or a possible broad C-peak) at $T = 297\text{K}$, where the lattice structure is the high-temperature tetragonal (HTT). Our obtained results at $T = 0.2J$ in Figs. 15(a) and 15(b) do not contradict with this experimental data for either FS, although we expect the realization of a ‘2dFS’ at $T = 297\text{K}$, since, according to our previous arguments¹⁴ (see §1), a q-1dFS may be realized in the presence of the LTT structure or its fluctuation,

2. ω -dependence and magnetic gap

The (single-layer) results, Figs. 5 and 7, have indicated that the positions of the sharp IC, DIC-peaks do not depend appreciably on ω up to $\omega \approx 0.1\text{--}0.2J$. Thus our results, including the energy scale, are consistent with experiments^{35,39,40}. One may recall a discussion in § 3.3 that in the presence of interlayer hopping, the precise values of η_{IC} in the u -RVB have been sensitive to ω especially for low $\delta (\lesssim 0.15)$. This sensitivity, however, has resulted from

the smearing of a hump structure of IC-peak with increasing ω , and the degree of change of η_{IC} is limited within the peak width. Such change may not be essential in comparison with experiments.

As shown in Fig. 10, with increasing ω , the degree of suppression by the d -wave gap is substantially weakened at the η_y -peak more than at the η_{xy} -peak. This is consistent with data by Lake *et al.*⁴¹. The argument in ref. 41 that the value of $\omega_{\text{mg}}(\mathbf{q})$ is momentum-independent, however, can not be understood within the present result where $\omega_{\text{mg}} \neq 0$ at the IC-peak while $\omega_{\text{mg}} = 0$ at the DIC-peak.

As for the value of ω_{mg} at the IC-peak, it has been reported that $\omega_{\text{mg}} = 6\text{--}7$ meV at $\delta = 0.15, 0.16, 0.18$ ^{40,41} and $\omega_{\text{mg}} = 0$ at $\delta = 0.10, 0.25$ ⁴⁰. The former data is consistent with the present result semiquantitatively as shown in Fig. 9, but the latter is not. For the data $\omega_{\text{mg}} = 0$ at $\delta = 0.25$, we note the experimental fact¹⁷ that the hole density is close to the phase boundary between the superconducting state and the metallic state. Because of such proximity to the normal state, (i) the value of ω_{mg} may be smaller than the present estimation (Fig. 9), and it may be difficult to observe such small ω_{mg} , and (ii) the fermion damping constant Γ may be larger than that in $\delta = 0.15\text{--}0.18$, which will smear the clear magnetic gap behavior as demonstrated in Fig. 8(a). To understand the data at $\delta = 0.10$, further detailed theoretical studies⁴² are required as to why static IC-AF order is stabilized at $\delta = 0.10$ ⁴³, 0.12 ^{44,45} and 0.13 ⁴³, since these static order will enhance the spectral weight near $\omega \approx 0$ meV to smear the magnetic gap.

3. Incommensurability versus hole density

Considering the experimental indication that the value of incommensurability observed by the *elastic* neutron scattering is almost the same with that by the *inelastic* one, we note the following experimental data: η_{IC} observed by the *inelastic* neutron scattering in LSCO^{17,46} at $T \approx T_c$ and by the *elastic* scattering in LNSCO^{47,48} below T_c , and η_{DIC} observed by the *elastic* scattering in LSCO^{49,50} at $T > T_c = 0$. Since our theory predicts the qualitatively different δ -dependence of η_{IC} and η_{DIC} between in the d -RVB state and in the u -RVB state (Fig. 13), the experimental data should be compared in either state. It is, however, not obvious which state should be taken. For the data taken at $T \gtrsim T_c$, there is a controversial issue whether the spin gap exists in LSCO^{35-38,40,52}. For the elastic data below T_c , it might

be reasonable to take the d -RVB state. However, the magnetic gap at the IC-peak in the d -RVB state is finite in the present theory while elastic data indicate that it is zero; we may not be limited to the d -RVB state at present. Thus, leaving these to future problems, we here make comparison with experimental data by taking both the d -RVB state and the u -RVB state.

In Figs. 13(a) and 13(b), we focus on the DIC-peak for $0.02 \lesssim \delta \lesssim 0.05$ and the IC-peak for $0.05 \lesssim \delta \lesssim 0.30$, although we have both the IC-peak and the DIC-peak at each δ in the present study. We see that for both state, the values of η_{IC} and η_{DIC} are somewhat smaller than the experimental values, but the semiquantitative agreement is obtained. More quantitative agreement may be obtained by the fine tuning of the FS, since as seen from Fig. 4, the value of incommensurability is sensitive to the position of the FS near $(\pi/2, \pi/2)$. In fact, we find that the FS used in the present analysis (Fig. 11) lies somewhat outer near $(\pi/2, \pi/2)$ compared with the position of the observed low-energy spectral weight³³, although we have fitted the FS near $(\pi, 0)$ and $(0, \pi)$ to the observed FS segments¹⁶.

The experimental data in LSCO by Yamada *et al.*¹⁷ show that the values of η_{IC} saturate in $\delta \gtrsim 0.15$. We have obtained similar possible saturation behavior in $0.15 \lesssim \delta \lesssim 0.20$ in the u -RVB state for $\omega = 0.01$ (Fig. 13(b)). As discussed in § 3.3, this possible saturation, however, has resulted from the fine structures of $\text{Im}\chi(\mathbf{q}, \omega)$ and is easily smeared out with increasing ω . It is beyond the present calculation to associate such subtle structures with the experimental data. We leave to a future study why the value of η_{IC} saturates at high δ in LSCO.

4. IC-peak versus DIC-peak

We have obtained both the IC-peak and the DIC-peak at each δ . Which peak should be observed experimentally? As shown in Figs. 12(b) and 12(d), the DIC-peak is substantially suppressed at high δ , which indicates that the IC-peak becomes dominant for high δ ($\gtrsim 0.20$). This is consistent with experiments^{17,47}. For lower δ , however, we expect both the IC-peak and the DIC-peak, and the former develops more rapidly than the latter with increasing ω . At present, we have no definite answer to the question why the IC-peak has been observed only in $\delta \gtrsim 0.05$ ^{17,47} and replaced by the DIC-peak in $0.02 \lesssim \delta \lesssim 0.05$ ⁴⁹⁻⁵¹.

B. Magnetic excitation in YBCO systems

We have seen in §3.4 that for the 2dFS (Fig. 16) the IC-peak is realized only in the d -RVB state and is replaced by the essentially C-peak in the u -RVB state within the ω -range studied here. This feature is consistent with experimental data for YBCO^{53–55}. Moreover, the 2dFS shown in Fig. 16 is consistent with the FS observed by ARPES⁵⁶. We therefore consider that magnetic excitation in YBCO systems may be understood on the basis of the 2dFS, as has been discussed theoretically^{27,57,58}.

C. Relation to ‘spin-charge stripes’ hypothesis

We have seen that fermiology can be a central concept for understanding magnetic excitation in high- T_c cuprates. This viewpoint contrasts with the ‘spin-charge stripes’ scenario^{1–3} where it is the formation of ‘charge stripes’, not effects of the FS, that gives rise to the magnetic IC,DIC-peaks.

Nonetheless, possible realization of the ‘charge stripes’ is interesting. In the present study, we have assumed that the charge density is uniform. When we relax this restriction, some kind of charge ordering may be stabilized in the state with a q-1dFS, which we are trying to clarify.

D. Degree of band anisotropy at high doping rate

In §2.1, we have fit a q-1dFS near $(\pi, 0)$ or $(0, \pi)$ to the observed FS segments by ARPES¹⁶. Figure 2 implies that band anisotropy remains even at high δ ($\gtrsim 0.20$). Such band anisotropy, however, can not be understood in terms of our previous arguments¹⁴ (see §1), since the crystal structure in LSCO with $\delta \gtrsim 0.20$ ¹⁷ is the HTT where we expect a ‘2dFS’. This problem should be resolved in a future.

V. SUMMARY

In the framework of the q-1d picture of the FS proposed by us, we have calculated $\text{Im}\chi(\mathbf{q}, \omega)$ in the ‘RPA’ within the slave-boson mean-field approximation to the t - J model. We have found that $\text{Im}\chi(\mathbf{q}, \omega)$ shows two kinds of sharp peaks, the IC-peak and the DIC-

peak, in both the u-RVB state and the d -RVB state. Their positions do not change appreciably with ω and the sharp peaks survive down to low δ . We have shown that the d -wave gap suppresses both the IC-peak and the DIC-peak, and that the former sees the magnetic gap ω_{mg} while the latter does not; interestingly the latter is more suppressed than the former for $\omega \gtrsim \omega_{\text{mg}}$. We have also performed calculations for the 2dFS, and have found that the IC,DIC-peaks are realized only in the d -RVB and are replaced by the essentially C-peak in the u-RVB. This feature is crucially different from the results for the q-1dFS. Taking these results, we have argued that essential features of magnetic excitation in LSCO systems can be understood in terms of the q-1d picture of the FS. Our scenario is different from the ‘spin-charge stripes’ scenario where it is the formation of ‘charge stripes’, not effects of the FS, that gives rise to the magnetic IC,DIC-peaks.

Acknowledgments

We thank H. Fukuyama for enlightening discussions and his continual encouragement. We also thanks H. Kimura, H. Kino, N. Ichikawa, M. Matsuda, M. Murakami, M. Saito, S. Uchida and K. Yamada for helpful discussions. This work is supported by a Grant-in-Aid for Scientific Research on Priority Areas from Ministry of Education, Culture, Sports, Science and Technology, Japan.

Appendix A: Formalism in Presence of Interlayer Hopping

We take a unit cell in which two CuO₂ planes, *A*-plane and *B*-plane in Fig. 1, are included, and separate the Bravais lattice into *A*-sublattice and *B*-sublattice. The *t*-*J* model with the interlayer hopping integral, *t*_⊥, is then given by

$$\begin{aligned}
 H = & - \sum_{i,j,\sigma}^A t^{(l)} f_{i\sigma}^{A\dagger} b_i^A b_j^{A\dagger} f_{j\sigma}^A + J \sum_{\langle i,j \rangle}^A \mathbf{S}_i^A \cdot \mathbf{S}_j^A \\
 & - \sum_{i,j,\sigma}^B t^{(l)} f_{i\sigma}^{B\dagger} b_i^B b_j^{B\dagger} f_{j\sigma}^B + J \sum_{\langle i,j \rangle}^B \mathbf{S}_i^B \cdot \mathbf{S}_j^B \\
 & - \sum_{i \in A, j \in B} t_{\perp} \left(f_{i\sigma}^{A\dagger} b_i^A b_j^{B\dagger} f_{j\sigma}^B + \text{h.c.} \right), \tag{A1}
 \end{aligned}$$

$$\begin{aligned}
 \sum_{\sigma} f_{i\sigma}^{A\dagger} f_{i\sigma}^A + b_i^{A\dagger} b_i^A = 1, \quad \sum_{\sigma} f_{i\sigma}^{B\dagger} f_{i\sigma}^B + b_i^{B\dagger} b_i^B = 1 \\
 \text{at each site of A and B-sublattices.} \tag{A2}
 \end{aligned}$$

We neglect the interlayer magnetic coupling *J*_⊥ whose order is estimated as $\sim 10^{-5} J^{30-32}$. Following the same procedure in §2.1, but adding the mean fields, $\langle \sum_{\sigma} f_{i\sigma}^{A\dagger} f_{j\sigma}^B \rangle$ and $\langle b_i^{A\dagger} b_j^B \rangle$, we obtain the mean-field Hamiltonian for the fermion part:

$$H_{\text{MF}} = \sum_{\mathbf{k}} \begin{pmatrix} f_{\mathbf{k}\uparrow}^{A\dagger} & f_{-\mathbf{k}\downarrow}^A & f_{\mathbf{k}\uparrow}^{B\dagger} & f_{-\mathbf{k}\downarrow}^B \end{pmatrix} \begin{pmatrix} \xi_{\mathbf{k}}^A & -\Delta_{\mathbf{k}} & \epsilon_{\mathbf{k}} & 0 \\ -\Delta_{\mathbf{k}} & -\xi_{\mathbf{k}}^A & 0 & -\epsilon_{\mathbf{k}} \\ \epsilon_{\mathbf{k}} & 0 & \xi_{\mathbf{k}}^B & -\Delta_{\mathbf{k}} \\ 0 & -\epsilon_{\mathbf{k}} & -\Delta_{\mathbf{k}} & -\xi_{\mathbf{k}}^B \end{pmatrix} \begin{pmatrix} f_{\mathbf{k}\uparrow}^A \\ f_{-\mathbf{k}\downarrow}^{A\dagger} \\ f_{\mathbf{k}\uparrow}^B \\ f_{-\mathbf{k}\downarrow}^{B\dagger} \end{pmatrix}, \tag{A3}$$

where

$$\xi_{\mathbf{k}}^A = F_x (\cos k_x + \alpha \cos k_y) + F' \cos k_x \cos k_y - \mu, \tag{A4}$$

$$\xi_{\mathbf{k}}^B = F_x (\alpha \cos k_x + \cos k_y) + F' \cos k_x \cos k_y - \mu, \tag{A5}$$

$$\Delta_{\mathbf{k}} = -\frac{3}{4} J \Delta_0 (\cos k_x - \cos k_y), \tag{A6}$$

$$\epsilon_{\mathbf{k}} = -8t_{\perp} \langle b_i^{A\dagger} b_j^B \rangle \cos \frac{k_x}{2} \cos \frac{k_y}{2} \cos \frac{k_z}{2}. \tag{A7}$$

(Note that \mathbf{k} is a 3-dimensional vector.) The form factor of $\epsilon_{\mathbf{k}}$ comes from the fact that *A*- and *B*-sublattices are relatively displaced by $[\frac{1}{2}, \frac{1}{2}, \frac{1}{2}]$ (tetragonal notation). We approximate $\langle b_i^{A\dagger} b_j^B \rangle \approx \delta$ and take the values of *F*_{*x*}, *F*' , Δ_0 , μ and α as the same ones determined in §2.1 for the band parameters, $t^{(1)}/J = 4$, $t^{(2)}/t^{(1)} = -1/6$ and $t^{(3)}/t^{(1)} = 0$. The value of *t*_⊥ is taken to be $0.05t^{(1)}$ so that band width of $\epsilon_{\mathbf{k}}$ is about 0.1 times that of $\xi_{\mathbf{k}}^A$ (or $\xi_{\mathbf{k}}^B$)²⁹.

Using the Hamiltonian eq. (A3), we obtain the irreducible dynamical magnetic susceptibility $\chi_0(\mathbf{q}, \omega)$:

$$\begin{aligned}
& \chi_0(\mathbf{q}, \omega) \\
= & \frac{1}{16NN_z} \sum_{\mathbf{k}} \left[C_{\mathbf{k}, \mathbf{k}+\mathbf{q}}^{1+} \left(\tanh \frac{\beta\lambda_{\mathbf{k}}^+}{2} - \tanh \frac{\beta\lambda_{\mathbf{k}+\mathbf{q}}^+}{2} \right) \frac{1}{\lambda_{\mathbf{k}}^+ + \omega + i\Gamma - \lambda_{\mathbf{k}+\mathbf{q}}^+} \right. \\
& + \frac{1}{2} C_{\mathbf{k}, \mathbf{k}+\mathbf{q}}^{1-} \left(\tanh \frac{\beta\lambda_{\mathbf{k}}^+}{2} + \tanh \frac{\beta\lambda_{\mathbf{k}+\mathbf{q}}^+}{2} \right) \left(\frac{1}{\lambda_{\mathbf{k}}^+ + \omega + i\Gamma + \lambda_{\mathbf{k}+\mathbf{q}}^+} + \frac{1}{\lambda_{\mathbf{k}}^+ - \omega - i\Gamma + \lambda_{\mathbf{k}+\mathbf{q}}^+} \right) \\
& + C_{\mathbf{k}, \mathbf{k}+\mathbf{q}}^{2+} \left(\tanh \frac{\beta\lambda_{\mathbf{k}}^-}{2} - \tanh \frac{\beta\lambda_{\mathbf{k}+\mathbf{q}}^-}{2} \right) \frac{1}{\lambda_{\mathbf{k}}^- + \omega + i\Gamma - \lambda_{\mathbf{k}+\mathbf{q}}^-} \\
& + \frac{1}{2} C_{\mathbf{k}, \mathbf{k}+\mathbf{q}}^{2-} \left(\tanh \frac{\beta\lambda_{\mathbf{k}}^-}{2} + \tanh \frac{\beta\lambda_{\mathbf{k}+\mathbf{q}}^-}{2} \right) \left(\frac{1}{\lambda_{\mathbf{k}}^- + \omega + i\Gamma + \lambda_{\mathbf{k}+\mathbf{q}}^-} + \frac{1}{\lambda_{\mathbf{k}}^- - \omega - i\Gamma + \lambda_{\mathbf{k}+\mathbf{q}}^-} \right) \\
& + C_{\mathbf{k}, \mathbf{k}+\mathbf{q}}^{3+} \left(\tanh \frac{\beta\lambda_{\mathbf{k}}^+}{2} - \tanh \frac{\beta\lambda_{\mathbf{k}+\mathbf{q}}^-}{2} \right) \left(\frac{1}{\lambda_{\mathbf{k}}^+ + \omega + i\Gamma - \lambda_{\mathbf{k}+\mathbf{q}}^-} + \frac{1}{\lambda_{\mathbf{k}}^+ - \omega - i\Gamma - \lambda_{\mathbf{k}+\mathbf{q}}^-} \right) \\
& \left. + C_{\mathbf{k}, \mathbf{k}+\mathbf{q}}^{3-} \left(\tanh \frac{\beta\lambda_{\mathbf{k}}^+}{2} + \tanh \frac{\beta\lambda_{\mathbf{k}+\mathbf{q}}^-}{2} \right) \left(\frac{1}{\lambda_{\mathbf{k}}^+ + \omega + i\Gamma + \lambda_{\mathbf{k}+\mathbf{q}}^-} + \frac{1}{\lambda_{\mathbf{k}}^+ - \omega - i\Gamma + \lambda_{\mathbf{k}+\mathbf{q}}^-} \right) \right] \quad (\text{A8})
\end{aligned}$$

where $2N_z$ (N) is the total number of CuO_2 planes (lattice sites in each CuO_2 plane) and \mathbf{k} -summation is taken in the region, $-\pi \leq k_x, k_y, k_z \leq \pi$, and

$$\lambda_{\mathbf{k}}^{\pm} = \sqrt{\left(\frac{\xi_{\mathbf{k}}^A + \xi_{\mathbf{k}}^B \pm \sqrt{D_{\mathbf{k}}}}{2} \right)^2 + \Delta_{\mathbf{k}}^2}, \quad (\text{A9})$$

$$D_{\mathbf{k}} = \left(\xi_{\mathbf{k}}^A - \xi_{\mathbf{k}}^B \right)^2 + 4\epsilon_{\mathbf{k}}^2, \quad (\text{A10})$$

and

$$C_{\mathbf{k}, \mathbf{k}+\mathbf{q}}^{1\pm} = \frac{1}{2} \left(1 + \frac{(\xi_{\mathbf{k}}^A - \xi_{\mathbf{k}}^B)(\xi_{\mathbf{k}+\mathbf{q}}^A - \xi_{\mathbf{k}+\mathbf{q}}^B) + 4\epsilon_{\mathbf{k}}\epsilon_{\mathbf{k}+\mathbf{q}}}{\sqrt{D_{\mathbf{k}}D_{\mathbf{k}+\mathbf{q}}}} \right) \times \left(1 \pm \frac{(\xi_{\mathbf{k}}^A + \xi_{\mathbf{k}}^B + \sqrt{D_{\mathbf{k}}})(\xi_{\mathbf{k}+\mathbf{q}}^A + \xi_{\mathbf{k}+\mathbf{q}}^B + \sqrt{D_{\mathbf{k}+\mathbf{q}}}) + 4\Delta_{\mathbf{k}}\Delta_{\mathbf{k}+\mathbf{q}}}{4\lambda_{\mathbf{k}}^+\lambda_{\mathbf{k}+\mathbf{q}}^+} \right) \quad (\text{A11})$$

$$C_{\mathbf{k}, \mathbf{k}+\mathbf{q}}^{2\pm} = \frac{1}{2} \left(1 + \frac{(\xi_{\mathbf{k}}^A - \xi_{\mathbf{k}}^B)(\xi_{\mathbf{k}+\mathbf{q}}^A - \xi_{\mathbf{k}+\mathbf{q}}^B) + 4\epsilon_{\mathbf{k}}\epsilon_{\mathbf{k}+\mathbf{q}}}{\sqrt{D_{\mathbf{k}}D_{\mathbf{k}+\mathbf{q}}}} \right) \times \left(1 \pm \frac{(\xi_{\mathbf{k}}^A + \xi_{\mathbf{k}}^B - \sqrt{D_{\mathbf{k}}})(\xi_{\mathbf{k}+\mathbf{q}}^A + \xi_{\mathbf{k}+\mathbf{q}}^B - \sqrt{D_{\mathbf{k}+\mathbf{q}}}) + 4\Delta_{\mathbf{k}}\Delta_{\mathbf{k}+\mathbf{q}}}{4\lambda_{\mathbf{k}}^-\lambda_{\mathbf{k}+\mathbf{q}}^-} \right) \quad (\text{A12})$$

$$C_{\mathbf{k}, \mathbf{k}+\mathbf{q}}^{3\pm} = \frac{1}{2} \left(1 - \frac{(\xi_{\mathbf{k}}^A - \xi_{\mathbf{k}}^B)(\xi_{\mathbf{k}+\mathbf{q}}^A - \xi_{\mathbf{k}+\mathbf{q}}^B) + 4\epsilon_{\mathbf{k}}\epsilon_{\mathbf{k}+\mathbf{q}}}{\sqrt{D_{\mathbf{k}}D_{\mathbf{k}+\mathbf{q}}}} \right) \times \left(1 \pm \frac{(\xi_{\mathbf{k}}^A + \xi_{\mathbf{k}}^B + \sqrt{D_{\mathbf{k}}})(\xi_{\mathbf{k}+\mathbf{q}}^A + \xi_{\mathbf{k}+\mathbf{q}}^B - \sqrt{D_{\mathbf{k}+\mathbf{q}}}) + 4\Delta_{\mathbf{k}}\Delta_{\mathbf{k}+\mathbf{q}}}{4\lambda_{\mathbf{k}}^+\lambda_{\mathbf{k}+\mathbf{q}}^-} \right) \quad (\text{A13})$$

The ‘RPA’ dynamical magnetic susceptibility is still given by eq. (13) and we set $r = 0.35$. The positive infinitesimal value of Γ is replaced with $0.01J$ as discussed in §2.2.

In the numerical calculation of eq. (A8), we keep $2N_z = 24$ CuO₂ planes to save computing time. The momentum k_z is then discrete with a interval $2\pi/N_z$. From the sequence of the calculations with $N_z = 1, 4, 8, 12, 25$, we expect that the overall \mathbf{q} -dependence of $\text{Im}\chi(\mathbf{q}, \omega)$, including the double-peak structures shown in Fig. 12(d), and the locations of the IC, DIC-peaks do not depend on N_z for $N_z \geq 8$.

Appendix B: Analytic Formulae for Incommensurability and Magnetic Gap

We give formulae to estimate the peak positions of $\text{Im}\chi(\mathbf{q}, \omega)$ for a single CuO₂ plane, namely the values of η_x and η_{xy} , at low ω and T . From eq. (14), the magnitude of the magnetic gap at η_y -peak is then calculated with such formulae.

One of the d -wave gap nodes on the FS is estimated to be $\mathbf{k}_{\text{node}} = -\frac{1}{2}(\pi - 2\pi\eta_{xy}, \pi - 2\pi\eta_{xy})$,

where

$$\sin(\pi\eta_{xy}) = \frac{F_x(1 + \alpha) + \sqrt{F_x^2(1 + \alpha)^2 + 4\mu F'}}{-2F'} . \quad (\text{B1})$$

The η_y -peak position with the scattering vector $\mathbf{q} = (\pi, \pi - 2\pi\eta_y)$ will be calculated by the minimum position of $\omega_{\text{mg}}(\mathbf{q}) = E_{\mathbf{q}+\mathbf{k}_{\text{node}}}$, namely $\frac{\partial\omega_{\text{mg}}(\mathbf{q})}{\partial\eta_y} = 0$. We then obtain

$$\sin(2\pi\eta_y - \pi\eta_{xy}) = \frac{(\alpha F_x - F' \sin(\pi\eta_{xy})) (F_x \sin(\pi\eta_{xy}) + \mu) - \frac{9}{16}\Delta_0^2 \sin(\pi\eta_{xy})}{(\alpha F_x - F' \sin(\pi\eta_{xy}))^2 + \frac{9}{16}\Delta_0^2} . \quad (\text{B2})$$

Numerical error of η_y (η_{xy}) is found to be less than $\sim 15\%$ ($\sim 1\%$) for $\delta \gtrsim 0.04$ and almost vanishes for $\delta \gtrsim 0.10$. Since we have checked that eqs. (B1) and (B2) reproduce the peak positions of $\text{Im}\chi_0(\mathbf{q}, \omega)$ quite well, the larger error at lower δ is understood as coming from the \mathbf{q} -dependence of the ‘RPA’ enhancement factor (denominator in eq. (13)), whose effects become prominent near the instability toward the antiferromagnetic long-range order.

The magnetic gap at η_y -peak is then calculated from eqs. (14), (B1) and (B2), and plotted as a function of δ in Fig. 9. It is seen that the analytical estimation reproduces the correct values (filled circles in Fig. 9) for $\delta \gtrsim 0.04$. The larger error at the lower δ is due to the numerical error of η_y .

Here we note that eq. (B2) will be reduced to

$$\sin(2\pi\eta_y - \pi\eta_{xy}) = \frac{F_x \sin(\pi\eta_{xy}) + \mu}{\alpha F_x - F' \sin(\pi\eta_{xy})} , \quad (\text{B3})$$

at high δ , since the band width ($\sim 2|F_x|$) becomes much larger than the d -wave singlet order Δ_0 . In fact, we find that the numerical error of η_y estimated by eq. (B3) is less than $\sim 5\%$ for $\delta \gtrsim 0.10$ and decreases to zero at the higher δ .

When we employ eqs. (B1) and (B3), eq. (14) is reduced to

$$\omega_{\text{mg}}(\mathbf{q}) = \frac{3}{4}J\Delta_0 (\sin(\pi\eta_{xy}) - \sin(\pi\eta_{xy} - 2\pi\eta_y)) . \quad (\text{B4})$$

This simple formula is reasonable at least for high δ ($\gtrsim 0.10$).

¹ J. M. Tranquada, B. J. Sternlieb, J. D. Axe, Y. Nakamura and S. Uchida: Nature **375** (1995) 561.

² J. M. Tranquada, J. D. Axe, N. Ichikawa, Y. Nakamura, S. Uchida and B. Nachumi: Phys. Rev. B **54** (1996) 7489.

- ³ J. M. Tranquada, J. D. Axe, N. Ichikawa, A. R. Moodenbaugh, Y. Nakamura and S. Uchida: Phys. Rev. Lett. **78** (1997) 338.
- ⁴ N. Ichikawa, S. Uchida, J. M. Tranquada, T. Niemöller, P. M. Gehring, S.-H. Lee and J. R. Schneider: Phys. Rev. Lett. **85** (2000) 1738.
- ⁵ M. V. Zimmermann, A. Vigliante, T. Niemöller, N. Ichikawa, T. Frello, J. Madsen, P. Wochner, S. Uchida, N. H. Andersen, J. M. Tranquada, D. Gibbs and J. R. Schneider: Europhys. Lett. **41** (1998) 629.
- ⁶ T. Niemöller, N. Ichikawa, T. Frello, H. Hünnefeld, N. H. Andersen, S. Uchida, J. R. Schneider and J. M. Tranquada: Eur. Phys. J. B **12** (1999) 509.
- ⁷ More precisely, the superlattice peaks are observed only at $(4\pi \pm 4\pi\delta, 0)$, and the extinction at $(4\pi, \pm 4\pi\delta)$ has been argued as due to structure factors².
- ⁸ V. J. Emery, S. A. Kivelson and O. Zacher: Phys. Rev. B **56** (1997) 6120.
- ⁹ S. A. Kivelson, E. Fradokin and V. J. Emery: Nature **393** (1998) 550.
- ¹⁰ M. I. Salkola, V. J. Emery and S. A. Kivelson: Phys. Rev. Lett. **77** (1996) 155.
- ¹¹ T. Tohyama, S. Nagai, Y. Shibata and S. Maekawa: Phys. Rev. Lett. **82** (1999) 4910.
- ¹² K. Machida and M. Ichioka: J. Phys. Soc. Jpn. **68** (1999) 2168; M. Ichioka and K. Machida: *ibid.* **68** (1999) 4020.
- ¹³ H. Yamase and H. Kohno: J. Phys. Soc. Jpn. **69** (2000) 332; H. Yamase, H. Kohno and H. Fukuyama: Physica B **284–288** (2000) 1375.
- ¹⁴ H. Yamase and H. Kohno: J. Phys. Soc. Jpn. **69** (2000) 2151.
- ¹⁵ H. Yamase, H. Kohno and H. Fukuyama: Physica C **341–348** (2000) 321.
- ¹⁶ A. Ino, C. Kim, T. Mizokawa, Z.-X. Shen, A. Fujimori, M. Takaba, K. Tamasaku, H. Eisaki and S. Uchida: J. Phys. Soc. Jpn. **68** (1999) 1496; A. Ino, C. Kim, M. Nakamura, T. Yoshida, T. Mizokawa, Z.-X. Shen, A. Fujimori, T. Kakeshita, H. Eisaki and S. Uchida: cond-mat/0005370.
- ¹⁷ K. Yamada, C. H. Lee, K. Kurahashi, J. Wada, S. Wakimoto, S. Ueki, H. Kimura, Y. Endoh, S. Hosoya, G. Shirane, R. J. Birgeneau, M. Greven, M. A. Kastner and Y. J. Kim: Phys. Rev. B **57** (1998) 6165.
- ¹⁸ M. K. Crawford, R. L. Harlow, E. M. McCarron, W. E. Farneth, J. D. Axe, H. Chou and Q. Huang: Phys. Rev. B **44** (1991) 7749.
- ¹⁹ B. Büchner, M. Breuer, A. Freimuth and A. P. Kampf: Phys. Rev. Lett. **73** (1994) 1841.
- ²⁰ S. Sakita, F. Nakamura, T. Suzuki and T. Fujita: J. Phys. Soc. Jpn. **68** (1999) 2755.

- ²¹ T. R. Thurston, R. J. Birgeneau, D. R. Gabbe, H. P. Jenssen, M. A. Kastner, P. J. Picone, N. W. Preyer, J. D. Axe, P. Böni, G. Shirane, M. Sato, K. Fukuda and S. Shamoto: Phys. Rev. B **39** (1989) 4327.
- ²² C. H. Lee, K. Yamada, M. Arai, S. Wakimoto, S. Hosoya and Y. Endoh: Physica C **257** (1996) 264.
- ²³ H. Kimura, K. Hirota, C. H. Lee, K. Yamada and G. Shirane: J. Phys. Soc. Jpn. **69** (2000) 851.
- ²⁴ C. J. Halboth and W. Metzner: Phys. Rev. Lett. **85** (2000) 5162.
- ²⁵ T. Tanamoto, H. Kohno and H. Fukuyama: J. Phys. Soc. Jpn. **61** (1992) 1886; *ibid.* **62** (1993) 717.
- ²⁶ We consider δ to be equal to the Sr^{2+} concentration, x .
- ²⁷ T. Tanamoto, H. Kohno and H. Fukuyama: J. Phys. Soc. Jpn. **62** (1993) 1455; *ibid.* **63** (1994) 2739.
- ²⁸ The magnetic gap is often referred to the ‘spin gap’. In this paper, however, we use the ‘spin gap’ as a terminology indicating the normal state gap.
- ²⁹ W. E. Pickett: Rev. Mod. Phys. **61** (1989) 433.
- ³⁰ C. J. Peters, R. J. Birgeneau, M. A. Kastner, H. Yoshizawa, Y. Endoh, J. Tranquada, G. Shirane, Y. Hidaka, M. Oda, M. Suzuki and T. Murakami: Phys. Rev. B **37** (1988) 9761.
- ³¹ T. Thio, T. R. Thurston, N. W. Preyer, P. J. Picone, M. A. Kastner, H. P. Jenssen, D. R. Gabbe, C. Y. Chen, R. J. Birgeneau and A. Aharony: Phys. Rev. B **38** (1988) 905.
- ³² K. B. Lyons, P. A. Fleury, J. P. Remeika, A. C. Cooper and T. J. Negran: Phys. Rev. B **37** (1988) 2353.
- ³³ X. J. Zhou, T. Yoshida, S. A. Kellar, P. V. Bogdanov, E. D. Lu, A. Lanzara, M. Nakamura, T. Noda, T. Kakeshita, H. Eisaki, S. Uchida, A. Fujimori, Z. Hussain and Z.-X. Shen: Phys. Rev. Lett. **86** (2001) 5578.
- ³⁴ G. Aeppli, T. E. Mason, S. M. Hayden, H. A. Mook and J. Kulda: Science **278** (1997) 1432.
- ³⁵ T. E. Mason, G. Aeppli and H. A. Mook: Phys. Rev. Lett. **68** (1992) 1414.
- ³⁶ T. Nakano, N. Momono, M. Oda and M. Ido: J. Phys. Soc. Jpn. **67** (1998) 2622.
- ³⁷ N. Momono, T. Matsuzaki, T. Nagata, M. Oda and M. Ido: J. Low Temp. Phys. **117** (1999) 353.
- ³⁸ S. Ohsugi, Y. Kitaoka, K. Ishida, G. Zheng and K. Asayama: J. Phys. Soc. Jpn. **60** (1991) 2351; *ibid.* **63** (1994) 700.

- ³⁹ M. Matsuda, K. Yamada, Y. Endoh, T. R. Thurston, G. Shirane, R. J. Birgeneau, M. A. Kastner, I. Tanaka and H. Kojima: *Phys. Rev. B* **49** (1994) 6958.
- ⁴⁰ C. H. Lee, K. Yamada, Y. Endoh, G. Shirane, R. J. Birgeneau, M. A. Kastner, M. Greven and Y.-J. Kim: *J. Phys. Soc. Jpn.* **69** (2000) 1170.
- ⁴¹ B. Lake, G. Aeppli, T. E. Mason, A. Schröder, D. F. McMorrow, K. Lefmann, M. Isshiki, M. Nohara, H. Takagi and S. M. Hayden: *Nature* **400** (1999) 43.
- ⁴² H. Yamase, H. Kohno, H. Fukuyama and M. Ogata: *J. Phys. Soc. Jpn.* **68** (1999) 1082; *J. Phys. Chem. Solids* **60** (1999) 1063.
- ⁴³ H. Matsushita, H. Kimura, M. Fujita, K. Yamada, K. Hirota and Y. Endoh: *J. Phys. Chem. Solids*. **60** (1999) 1071.
- ⁴⁴ T. Suzuki, T. Goto, K. Chiba, T. Shinoda, T. Fukase, H. Kimura, K. Yamada, M. Ohashi and Y. Yamaguchi: *Phys. Rev. B* **57** (1998) R3229.
- ⁴⁵ H. Kimura, K. Hirota, H. Matsushita, K. Yamada, Y. Endoh, S. H. Lee, C. F. Majkrzak, R. Erwin, G. Shirane, M. Greven, Y. S. Lee, M. A. Kastner and R. J. Birgeneau: *Phys. Rev. B* **59** (1999) 6517.
- ⁴⁶ K. Yamada: private communications.
- ⁴⁷ N. Ichikawa: Doctor Thesis, University of Tokyo, Tokyo, 1999.
- ⁴⁸ N. Ichikawa: private communications.
- ⁴⁹ S. Wakimoto, R. J. Birgeneau, M. A. Kastner, Y. S. Lee, R. Erwin, P. M. Gehring, S. H. Lee, M. Fujita, K. Yamada, Y. Endoh, K. Hirota and G. Shirane: *Phys. Rev. B* **61** (2000) 3699.
- ⁵⁰ M. Matsuda, M. Fujita, K. Yamada, R. J. Birgeneau, M. A. Kastner, H. Hiraka, Y. Endoh, S. Wakimoto and G. Shirane: *Phys. Rev. B* **62** (2000) 9148.
- ⁵¹ M. Fujita, K. Yamada, H. Hiraka, P. M. Gehring, S. H. Lee, S. Wakimoto and G. Shirane: *cond-mat/010320*.
- ⁵² H. Fukuyama: *J. Phys. Chem. Solids* **59** (1998) 447.
- ⁵³ P. Dai, H. A. Mook and F. Dögan: *Phys. Rev. Lett.* **80** (1998) 1738.
- ⁵⁴ M. Arai, T. Nishijima, Y. Endoh, T. Egami, S. Tajima, K. Tomimoto, Y. Shiohara, M. Takahashi, A. Garrett and S. M. Bennington: *Phys. Rev. Lett.* **83** (1999) 608.
- ⁵⁵ P. Bourges, Y. Sidis, H. F. Fong, L. P. Regnault, J. Bossy, A. Ivanov and B. Keimer: *Science* **288** (2000) 1234.
- ⁵⁶ M. C. Schabel, C.-H. Park, A. Matsuura, Z.-X. Shen, D. A. Bonn, Ruixing Liang and W. N.

Hardy: Phys. Rev. B **57** (1998) 6107.

⁵⁷ J. Brinckmann and P. A. Lee: Phys. Rev. Lett. **82** (1999) 2915.

⁵⁸ Q. Si, Y. Zha, K. Levin and J. P. Lu: Phys. Rev. B **47** (1993) 9055; Y. Zha, K. Levin and Q. Si: *ibid.* **47** (1993) 9124; D. Z. Liu, Y. Zha and K. Levin: Phys. Rev. Lett. **75** (1995) 4130; Y.-J. Kao, Q. Si and K. Levin: Phys. Rev. B **61** (2000) R11898.